metals

MDPI

Article

Detoxification-Oriented Carbonate Leaching of Selenium and Tellurium from Lead-Rich Fly Ash: Experimental and Kinetic Analysis

Majid Ramezanpour Aghdami, Ashkan Mohammad Beygian and Eskandar Keshavarz Alamdari *

Department of Materials and Metallurgical Engineering, Amirkabir University of Technology, No. 350, Hafez Ave, Valiasr Square, Tehran 1591634311, Iran; majidaghdamy@gmail.com (M.R.A.); ashkanmb@aut.ac.ir (A.M.B.)
* Correspondence: alamdari@aut.ac.ir; Fax: +98-21-6696-7408

Abstract

Copper anodic slime is often smelted with lead to improve silver and gold recovery, generating a fine lead-rich fly ash that contains notable amounts of selenium and tellurium. Due to its high lead content and sub-micron particle size, this residue poses significant environmental and occupational health risks. This study evaluates sodium carbonate (Na_2CO_3) leaching as an environmentally benign pre-treatment aimed at partially removing selenium and tellurium while stabilizing lead through carbonate formation. The goal is detoxification rather than maximum metal recovery, enabling safer disposal or subsequent recycling. A central composite design (CCD) in Design-Expert software (Version 12) was used to assess the effects of Na_2CO_3 concentration, temperature, solid-to-liquid ratio, and time on selenium and tellurium dissolution. Selenium recovery reached up to 53.9%, while tellurium recovery peaked at approximately 33.9%. Scanning electron microscopy showed the dust to consist mainly of semi-spherical and elongated particles, with lead carbonate forming preferentially on particle surfaces during leaching. Energy-dispersive spectroscopy confirmed conversion of lead sulfate phases to lead carbonate, which increasingly restricted selenium and tellurium dissolution. Kinetic evaluation suggested selenium leaching follows mixed control involving both surface reaction and diffusion through product layers, whereas tellurium dissolution lacked consistent kinetic behavior. Thermodynamic calculations supported the stabilization of lead as cerussite ($PbCO_3$), indicating improved environmental safety. The overall dissolution trends were successfully represented using an apparent Shrinking Core Model (SCM) based on measurements collected at 20 °C, 60 °C, and 100 °C.

Keywords: selenium; tellurium; lead-rich fly ash; sodium carbonate leaching; product-layer diffusion; copper anode slime residue; detoxification

Check for updates

Academic Editors: Yang Tian and Qingchun Yu

Received: 15 March 2026
Revised: 10 April 2026
Accepted: 15 April 2026
Published: 21 April 2026

Copyright: © 2026 by the authors. Licensee MDPI, Basel, Switzerland. This article is an open access article distributed under the terms and conditions of the Creative Commons Attribution (CC BY) license.

1. Introduction

Selenium and tellurium are group-16 chalcogens with chemical behaviors similar to sulfur, often exhibiting comparable reaction pathways in metallurgical systems [1]. Their strategic importance has grown in recent decades, particularly due to expanding photovoltaic applications; tellurium availability is considered a potential constraint for large-scale cadmium telluride (CdTe) thin-film solar cell production, with the photovoltaic sector currently consuming about 26% of global tellurium output [2] and projections suggesting that up to 90% may be directed to CdTe technologies by the end of the 21st century [3].

Selenium is also used in photovoltaic devices and remains important in pigments, ceramics, glass decolorization, and metallurgy [4]. Because primary ores of selenium and tellurium are rare, most global production originates from secondary sources such as copper anodic slime formed during electrolytic copper refining [1,5], where concentrations may reach 46 wt.% selenium and 4 wt.% tellurium depending on ore mineralogy [6]. Mineralogical studies show that copper selenides and tellurides can react during silver dissolution and later precipitate as ringed or semi-ringed structures that trap valuable phases and impede recovery [7]. Their stability across pH conditions further indicates solubility in alkaline media, while tellurium can be selectively precipitated near pH 5, providing opportunities for separation from selenium [8].

A variety of pyrometallurgical and hydrometallurgical methods has been developed for extracting selenium and tellurium from copper anodic slime, including soda roasting, pressure leaching, acidic leaching with oxidants, sulfation roasting, and chlorination, each offering distinct benefits and drawbacks [4]. Soda roasting with sodium carbonate followed by sulfuric acid leaching can recover up to 90% of tellurium from copper telluride slags [9], while alkaline roasting with sodium carbonate and subsequent autoclave leaching in NaOH has similarly achieved tellurium recoveries near 90%, with high-purity metal obtained by electrowinning [10]. To further elucidate the operational and environmental distinctions between these approaches, a comparative summary of the pyrometallurgical and hydrometallurgical routes is provided in Appendix A (Table A1). Pressure leaching in sulfuric acid with oxidants such as hydrogen peroxide or oxygen has also produced high selenium and tellurium recoveries [11,12]. Acidic leaching systems combining sulfuric acid with oxidizing agents have been widely studied, yielding over 85% recovery from selenium distillation residues using oxygen injection and hydrogen peroxide [13], and high tellurium recovery from Te–Bi ores using ferric ions as oxidants [14]. Synergistic H_2SO_4–H_2O_2 systems have enabled up to 93.6% selenium recovery from anodic slime [15] and approximately 97% tellurium recovery alongside copper dissolution [16]. Alkaline leaching approaches have likewise shown promise: up to 86% selenium dissolution in NaOH with oxygen and potassium permanganate [17], selective tellurium dissolution using sodium cyanide with higher efficiency for TeO_2 than elemental Te [18], effective tellurium extraction using sodium sulfide [19], around 85% tellurium recovery in NaOH after sulfation roasting [8], and more than 90% recovery from copper telluride precipitates using NaOH with hydrogen peroxide [20].

Beyond recovery efficiency, several investigations have focused on the kinetics of selenium and tellurium leaching. Selenium dissolution from copper anodic slime using nitric and sulfuric acids has been reported to proceed through two kinetic regimes, with chemical reaction control at early stages and mixed diffusion–reaction control at later stages [21]. Pan et al. demonstrated that selenium leaching from acid sludge in NaOH–H_2O_2 systems follows a homogeneous reaction kinetic model [22]. Kinetic studies on tellurium-bearing materials using Na_2S–NaOH solutions have shown that tellurium dissolution can be described by the Avrami equation, indicating mixed diffusion and chemical reaction control [23]. Similar conclusions were drawn for tellurium leaching from copper anodic slime in sulfuric acid systems using graphite and permanganate as additives, while selenium dissolution in the same system was predominantly controlled by chemical reactions [24]. Selective tellurium leaching from copper anodic slime using Na_2S media has also been reported to follow an Avrami-type kinetic model with product-layer diffusion as the rate-limiting step [25].

Despite the extensive body of work on copper anodic slime, relatively little attention has been paid to secondary residues generated during downstream processing of these materials. In several industrial flowsheets, including those reported by Moosavi et al. [26],

copper anodic slime is smelted together with lead to facilitate the recovery of silver and gold. This practice results in the formation of a fine, lead-rich fly ash containing significant amounts of selenium, tellurium, and antimony. Such residues consist of sub-micron particles and pose serious environmental and occupational health risks if not properly treated. Industrial examples of this processing route can be found in copper-refining operations in Iran, where the generated fly ash requires stabilization prior to disposal or recycling. Exposure to high levels of lead is known to cause severe neurological damage, particularly in children [27], while occupational exposure to selenium-bearing dusts may result in respiratory irritation and bronchial effects [28]. Exposure to tellurium has also been associated with gastrointestinal symptoms and characteristic garlic-like breath [29].

The present study departs from conventional efforts that focus on maximizing selenium and tellurium recovery from copper anodic slime by instead developing a detoxification-oriented pre-treatment for hazardous lead-rich fly ash generated during high-temperature smelting. This previously unexamined sub-micron dust contains high levels of lead and volatile chalcogen species, posing serious environmental and occupational risks. Sodium carbonate leaching is applied not to achieve complete metal extraction but to stabilize lead through carbonate formation while partially mobilizing selenium and tellurium into a manageable aqueous phase. Detoxification efficiency, residue stability, and recyclability are therefore prioritized over recovery yield. Microscopic characterization and kinetic analysis reveal key phase transformations, particle-scale dissolution processes, and rate-controlling mechanisms, enabling a deeper understanding of how leaching behavior influences detoxification outcomes. By connecting dissolution kinetics with residue stabilization rather than metal recovery alone, this study establishes a physically grounded framework for defining practical operating conditions that support safer handling, recycling, or disposal of lead-rich metallurgical dusts.

2. Materials and Methods

A lead-rich fly ash containing selenium and tellurium was obtained from a small-scale metallurgical processing plant located near Tehran, Iran. This material represents a secondary hazardous residue generated during high-temperature lead smelting of copper anodic slime for precious-metal recovery. Prior to this study, the fly ash had been subjected to sulfuric acid leaching at the plant with the aim of maximizing selenium and tellurium recovery; however, a considerable fraction of these elements remained in the solid residue.

Upon receipt, the samples were dried at 100 °C to remove residual moisture, followed by grinding and sieving to break agglomerates and ensure homogeneity. The chemical composition of the pre-leached sample was determined by ICP-OES (VISTA-PRO, VARIAN, Palo Alto, CA, USA), and the results are presented in Table 1.

Table 1. ICP analysis of pre-leached sample.

Components	Pb	S	Se	As	Sb	Te	Zn	Fe
Wt %	63.2	28.5	2.7	2.2	1.3	1.1	0.5	0.3

Phase identification was carried out using X-ray diffraction (XRD, PHILIPS PW1730, Amsterdam, The Netherlands) with a step size of 0.05°, time per step of 1s and angles ranging from 10° to 80°. The XRD pattern (Figure 1) indicates that selenium and tellurium are predominantly present in oxidized forms associated with lead phases. This observation implies that disruption of Pb–Se and Pb–Te associations is a prerequisite for selenium and tellurium mobilization. Both selenium and tellurium were identified mainly in hexavalent states.

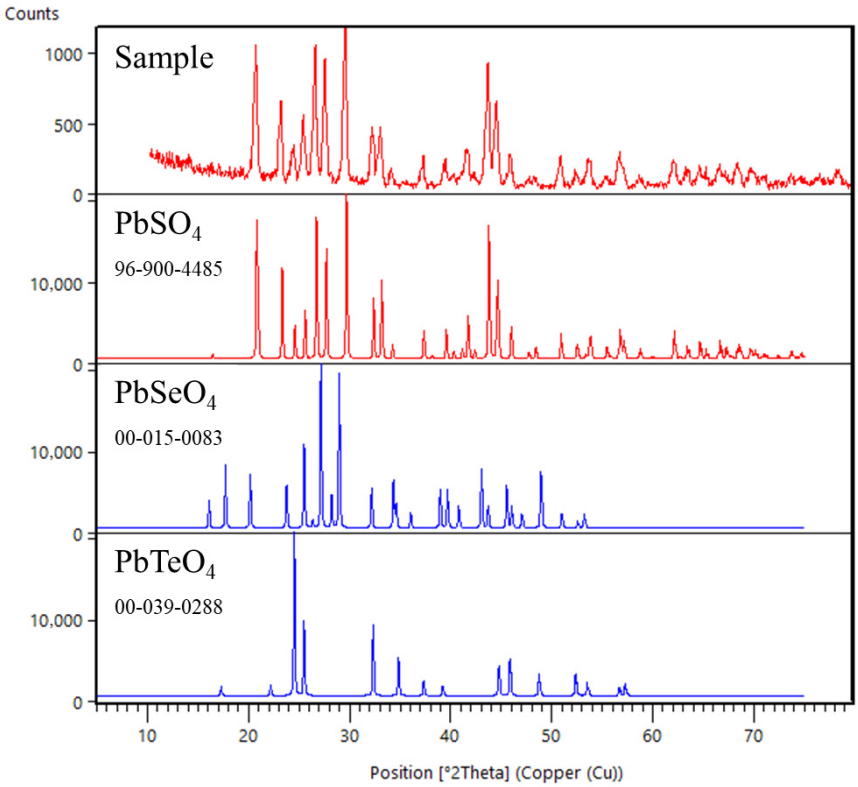

Figure 1. XRD analysis of pre-leached sample.

All leaching experiments were conducted using aqueous sodium carbonate (Na_2CO_3) (Merck, Darmstadt, Germany) solutions prepared from analytical-grade reagent and deionized water. The selection of Na_2CO_3 was motivated by its ability to stabilize lead as insoluble carbonate over a wide pH range, as reported by Arai et al. [30]. In carbonate media, lead sulfate and lead selenate phases are expected to transform into lead carbonate while selenium and tellurium are transferred into soluble sodium salts, thereby enabling selective detoxification of the residue.

The following reactions are considered thermodynamically favorable in Na_2CO_3 solution:

$$PbSO_4(s) + Na_2CO_3 \rightarrow PbCO_3(s) + Na_2SO_4 \quad (1)$$

$$PbSeO_4(s) + Na_2CO_3 \rightarrow PbCO_3(s) + Na_2SeO_4 \quad (2)$$

$$PbTeO_4(s) + Na_2CO_3 \rightarrow PbCO_3(s) + Na_2TeO_4 \quad (3)$$

According to HSC Chemistry, the standard Gibbs free energies at room temperature are -34.4 kJ mol^{-1} and -20.2 kJ mol^{-1} for the first and second reactions, respectively, indicating high thermodynamic feasibility. Although thermodynamic data for the tellurate reaction are not available, similar behavior is expected due to the chemical analogy between selenium and tellurium. The precipitated lead carbonate can be readily recycled to metallic lead using established metallurgical routes [31].

2.1. Experimental Procedure

Leaching experiments were carried out in a 1 L glass reactor (omsons, Hennef, Germany) operated in batch mode, with a constant working volume of 500 mL. Agitation was provided by a mechanical stirrer (IKA microstar 150, Staufen, Germany) at 200 rpm to ensure homogeneous suspension of solids. Temperature was controlled using a thermostated water bath, and a condenser was employed to prevent solution loss at elevated temperatures. A schematic of the experimental setup is shown in Figure 2.

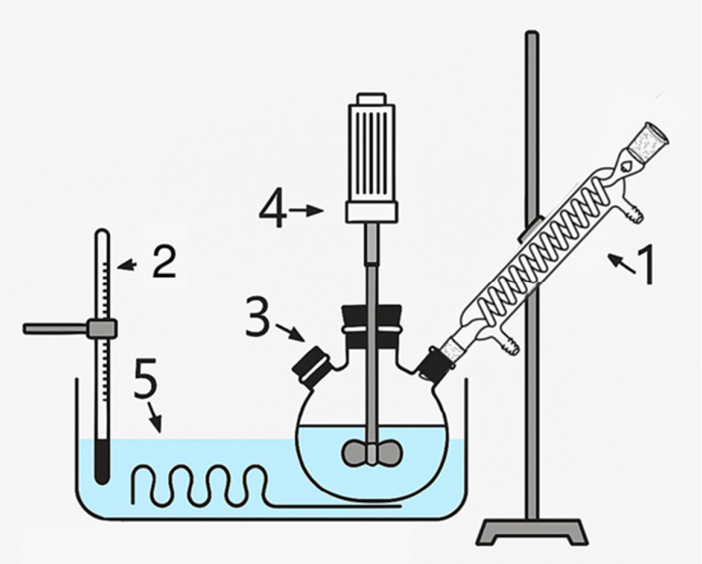

Figure 2. Equipment used for conducting tests: a condenser (1), thermometer (2), flask (3), stirrer (4), and water bath with controlled temperature (5) can be seen.

All solid materials were weighed using an analytical balance with a precision of 0.001 g (Sartorius, Göttingen, Germany), and solutions were prepared using volumetric flasks (Omsons, Hennef, Germany) to minimize experimental error. Preliminary experiments indicated that increasing Na_2CO_3 concentration up to 1 mol L^{-1} enhanced selenium and tellurium dissolution, while higher concentrations resulted in no significant additional benefit. Importantly, lead remained insoluble under all tested conditions, consistent with the literature reports [30]. Solid-to-liquid ratios and leaching times were selected based on process practicality and the results of preliminary tests, with emphasis on defining a feasible detoxification-oriented operational window rather than maximizing extraction.

2.2. Experimental Design and Kinetic Sampling

The experimental matrix was designed using Design Expert® software (version 12), applying a central composite design (CCD) to evaluate the effects of four variables: sodium carbonate concentration, temperature, solid-to-liquid ratio, and leaching time. Similar statistical approaches have been successfully applied in hydrometallurgical studies to analyze multivariable systems [32,33]. The design consisted of 24 factorial points and 6 center points, resulting in a total of 30 experimental conditions. The variable ranges and levels are summarized in Table 2.

Table 2. Variable values for central composition design.

		Level				
Variables	**Symbols**	**−2**	**−1**	**0**	**1**	**2**
Sodium carbonate concentration (mol/Lit)	$[Na_2CO_3]$	0.1	0.3	0.5	0.7	0.9
Temperature (°C)	T	20	40	60	80	100
Solid-to-liquid ratio (gr/mlit)	s/L	0.025	0.05	0.075	0.1	0.125
Time (min)	t	15	30	45	60	75

Based on this design, 20 leaching experiments were performed. During each experiment, solution samples were withdrawn at 15 min intervals (five samples per run) to capture both the initial rapid dissolution stage and the subsequent slower regime. Sampling

was conducted using 5 mL syringes, and the solutions were filtered through syringe filters to remove suspended solids. The samples were diluted 100-fold and analyzed by ICP OES. It should be noted that the target element concentrations in the diluted samples remained well above the standard instrumental limits of detection (LOD) and fell entirely within the optimal linear calibration range of the instrument, thereby ensuring the analytical reliability of the kinetic measurements without operating near trace-level thresholds.

The resulting concentration–time data were used for kinetic evaluation and to assess selenium and tellurium mobilization efficiency. Both recovery and final solution concentration were considered as response variables. The experimental conditions corresponding to the conducted runs are listed in Table 3.

Table 3. Conducted test parameters.

Run	S/L	Concentration	Temperature
	(%(10^2 × (g/mL))	(mol/L)	(°C)
1	7.5	0.5	20
2	5	0.7	80
3	7.5	0.5	100
4	10	0.3	80
5	7.5	0.5	60
6	5	0.3	80
7	12.5	0.5	60
8	2.5	0.5	60
9	7.5	0.5	60
10	10	0.3	40
11	7.5	0.5	60
12	7.5	0.1	60
13	7.5	0.5	60
14	7.5	0.9	60
15	5	0.3	40
16	10	0.7	80
17	7.5	0.5	60
18	7.5	0.5	60
19	10	0.7	40
20	5	0.7	40

3. Results and Discussion

3.1. Characterization of Lead-Rich Fly Ash and Initial Microstructural Evolution

Scanning electron microscopy (ESEM, FEI Quanta 200, Hillsboro, OR, USA) was employed to characterize the pristine lead-rich fly ash and to investigate the initial microstructural changes induced by sodium carbonate leaching. Representative SEM micrographs of the untreated material and selected leached residues are presented in Figure 3.

An unavoidable agglomeration can be observed in The pre-leached fly ash, which consists predominantly of fine particles exhibiting semi-spherical and elongated morphologies (Figure 3A). Quantitative particle size analysis, performed on more than 30 representative particles using image analysis software (ImageJ 1.52v, National Institutes of Health (NIH)), indicates average diameters of approximately 300 nm for semi-spherical particles and about 800 nm for elongated particles. These numbers change to 200 nm and 1200 nm, respectively, after leaching. Such fine particle sizes and irregular morphologies are characteristic of secondary particulates generated during high-temperature copper smelting and anodic slime processing and are known to contribute to the high reactivity and environmental risk associated with these residues. To qualitatively evaluate the morphological evolution, image analysis was conducted on selected representative particles (over 30 particles) us-

ing ImageJ software. While this does not represent a statistically absolute particle size distribution, this estimative approach evidently highlights the morphological shift from pseudo-spherical to elongated shapes during the leaching process.

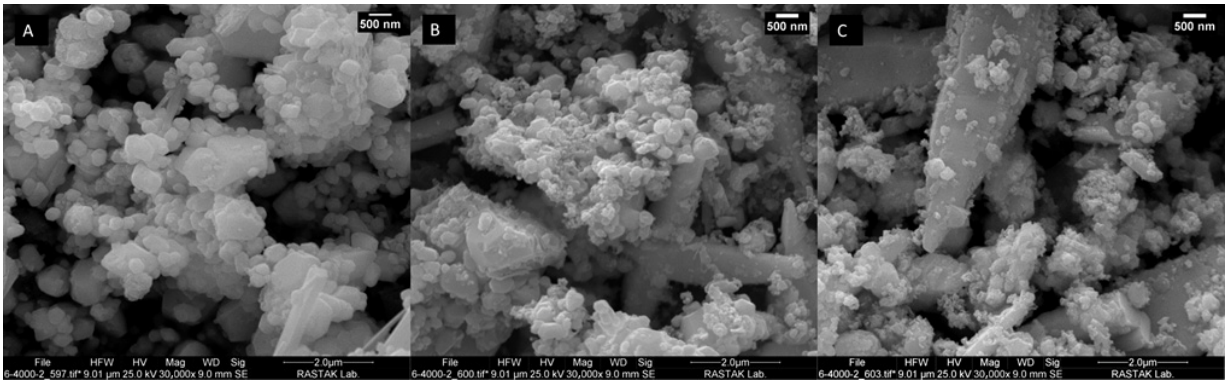

Figure 3. SEM Images of leaching residues based on samples: pre-leached sample (**A**), test number 10 residue (**B**), and test number 17 residue (**C**). Magnification for these images was set at 30,000×.

Following sodium carbonate leaching, pronounced microstructural changes are observed (Figure 3B,C). A progressive reduction in the size of semi-spherical particles is evident, whereas elongated particles persist and, in some cases, exhibit an apparent increase in relative size. This non-uniform morphological evolution suggests that leaching proceeds via preferential surface reactions affecting specific particle populations rather than through homogeneous dissolution of the entire solid matrix.

Energy-dispersive X-ray spectroscopy (EDS) analyses (Z2e, AMETEC, Berwyn, PA, USA) of the untreated fly ash, quantitatively summarized in Table 4 and illustrated by the corresponding SEM images and EDS spectra in Figure 4, confirm a lead-rich composition, with selenium and tellurium present as minor constituents associated with Pb-bearing phases. After leaching, while Pb content in spherical particles is relatively similar to pre-leach values, there is a rise in Pb content in elongated particles. This and the decreased amount of both sulfur and oxygen suggest that elongated particles were more favorable for $PbCO_3$ to precipitate. $PbCO_3$ crystals may cover $PbTeO_3$, $PbTeO_4$, $PbSeO_3$, and $PbSeO_4$ crystals on elongated particles, reducing Se and even stopping Te dissolution. A comparison between pre- and post-leaching elongated particle size will result in a 200 nm estimate for the thickness of this passive layer.

Table 4. EDS analysis of pre-leached samples.

Element	Pb	O	S	Se	Te	Sb
Wt(%)	76.5	7.98	7.8	5.71	1.03	0.95

Relative lead enrichment accompanied by changes in oxygen and sulfur signals indicates the initiation of secondary phase formation on particle surfaces, consistent with the precipitation of lead carbonate species as also supported by XRD results.

Overall, the observed early-stage microstructural and compositional evolution indicates the onset of a surface-controlled process. The formation of Pb-rich surface layers is expected to influence subsequent leaching behavior by altering mass-transfer pathways and restricting further dissolution of associated chalcogen elements. This characterization therefore establishes the structural foundation for interpreting the detoxification-oriented leaching behavior discussed in the following section.

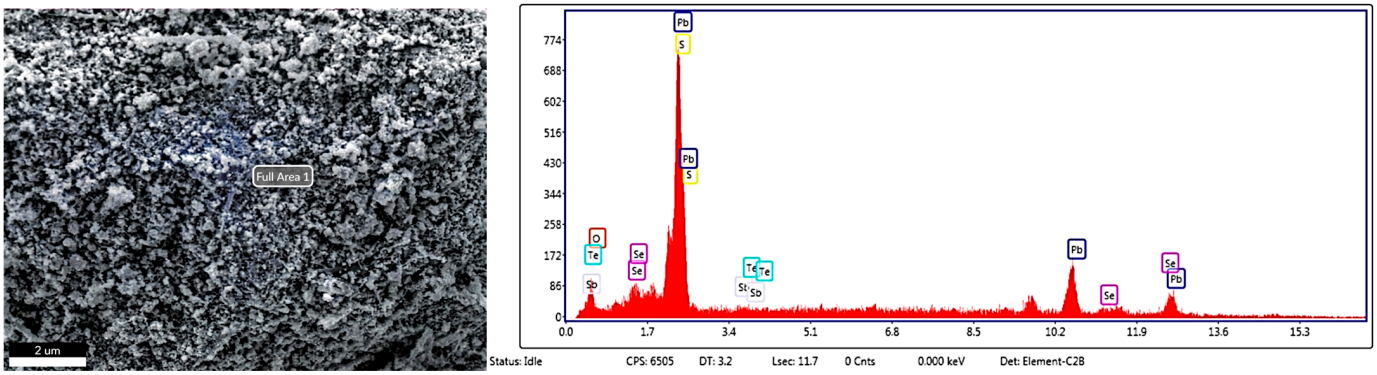

(**A**) (**B**)

Figure 4. SEM imaging (**A**) and peaks diagram (**B**) for pre-leached samples.

3.2. Detoxification-Oriented Leaching Behavior of Selenium and Tellurium

Selenium and tellurium dissolution behaviors during sodium carbonate leaching were systematically evaluated to assess the effectiveness of the process from a detoxification perspective rather than conventional metal recovery. The quantitative leaching results obtained under different experimental conditions are summarized in Tables 5 and 6, while the corresponding microstructural and compositional evidence supporting the observed trends is provided by Figure 5 and Table 7.

Table 5. Total Se concentration and recovery data relative to time.

	Se Concentration					Se Recovery				
Run	**Time (min)**					**Time (min)**				
	15	**30**	**45**	**60**	**75**	**15**	**30**	**45**	**60**	**75**
1	330.8	286.5	301.8	292.0	346.0	21.3	21.8	22.5	24.6	25.8
2	355.5	383.8	391.8	457.5	477.5	39.7	42.9	43.8	51.1	53.4
3	502.3	604.5	654.5	690.5	723.0	37.4	45.0	48.8	51.4	53.9
4	434.0	501.8	397.5	524.5	512.5	24.2	28.0	22.2	29.3	28.6
5	375.8	424.5	444.8	456.3	475.8	28.0	31.6	33.1	34.0	35.4
6	309.5	330.8	348.0	379.0	406.0	34.6	37.0	38.9	42.3	45.4
7	644.3	746.0	775.5	846.0	964.0	28.8	33.3	34.7	37.8	43.1
8	174.8	196.8	214.8	214.0	240.8	39.1	44.0	48.0	47.8	53.8
9	466.3	583.8	615.0	641.3	659.3	34.7	43.5	45.8	47.8	49.1
10	304.3	361.8	394.5	418.0	431.8	17.0	20.2	22.0	23.4	24.1
11	442.0	480.8	520.8	555.0	619.5	32.9	35.8	38.8	41.3	46.1
12	147.0	172.5	240.3	160.3	167.0	10.9	12.8	17.9	11.9	12.4
13	381.8	416.3	481.5	540.0	542.0	28.4	31.0	35.9	40.2	40.4
14	427.8	482.8	523.0	526.5	583.3	31.9	36.0	39.0	39.2	43.4
15	162.3	185.5	209.0	207.5	242.0	18.1	20.7	23.4	23.2	27.0
16	688.5	763.8	824.5	892.3	870.3	38.5	42.7	46.1	49.8	48.6
17	404.3	476.0	511.0	519.3	566.3	30.1	35.5	38.1	38.7	42.2
18	392.3	479.8	481.3	561.8	580.0	29.2	35.7	35.8	41.8	43.2
19	366.5	416.0	480.8	513.0	540.0	20.5	23.2	26.9	28.7	30.2
20	207.5	310.0	336.5	357.0	368.0	23.2	34.6	37.6	39.9	41.1

Table 6. Total Te concentration and recovery data relative to time.

Run	Te Concentration (ppm)					Te Recovery (%)				
	Time (min)					Time (min)				
	15	**30**	**45**	**60**	**75**	**15**	**30**	**45**	**60**	**75**
1	7.3	5.5	4.8	Nd	6.5	1.1	0.8	0.7	Nd	1.0
2	101.5	104.0	111.8	150.8	151.5	22.7	23.2	25.0	33.7	33.9
3	100.0	113.5	89.3	145.5	161.5	14.9	16.9	13.3	21.7	24.1
4	3.3	24.0	11.8	16.0	9.8	0.4	2.7	1.3	1.8	1.1
5	61.3	78.5	85.3	54.8	97.8	9.1	11.7	12.7	8.2	14.6
6	36.5	68.0	54.3	78.8	57.8	8.2	15.2	12.1	17.6	12.9
7	34.3	37.8	34.3	29.3	29.0	3.1	3.4	3.1	2.6	2.6
8	51.5	60.5	81.3	71.8	71.5	23.0	27.0	36.3	32.1	32.0
9	71.3	110.0	125.5	92.5	93.5	10.6	16.4	18.7	13.8	13.9
10	nd	nd	nd	Nd	Nd	nd	nd	nd	Nd	Nd
11	65.5	80.8	91.3	90.3	150.3	9.8	12.0	13.6	13.4	22.4
12	nd	nd	6.3	Nd	8.8	nd	nd	0.9	Nd	1.3
13	37.3	48.0	71.3	76.0	75.3	5.5	7.2	10.6	11.3	11.2
14	102.3	80.3	107.3	119.3	130.8	15.2	12.0	16.0	17.8	19.5
15	10.5	18.0	12.3	16.0	18.3	2.3	4.0	2.7	3.6	4.1
16	128.5	145.3	179.5	174.5	159.5	14.4	16.2	20.1	19.5	17.8
17	62.8	70.8	66.8	68.3	76.0	9.3	10.5	9.9	10.2	11.3
18	44.8	44.5	57.5	57.5	75.0	6.7	6.6	8.6	8.6	11.2
19	43.5	45.5	60.3	54.8	65.3	4.9	5.1	6.7	6.1	7.3
20	73.0	60.8	71.5	78.8	77.0	16.3	13.6	16.0	17.6	17.2

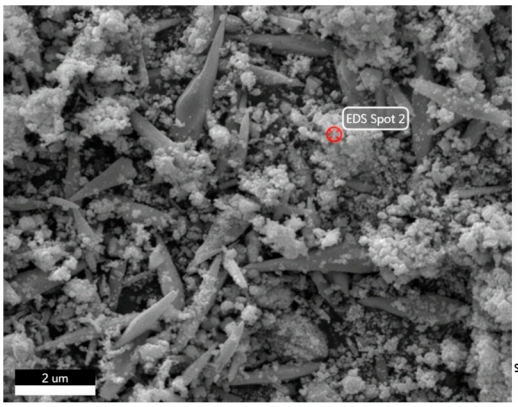

(**A**)

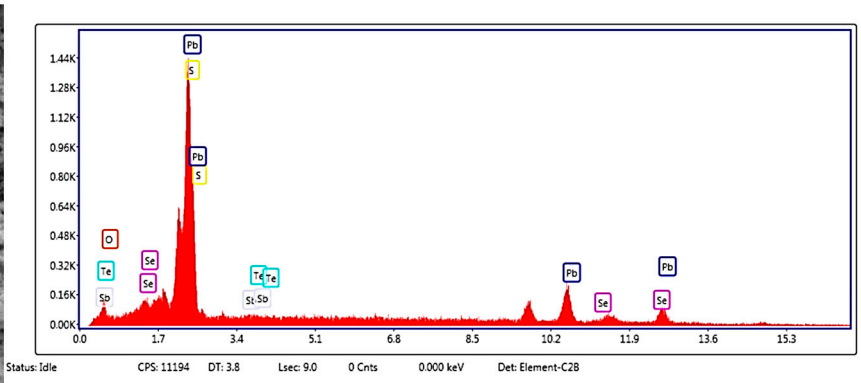

(**B**)

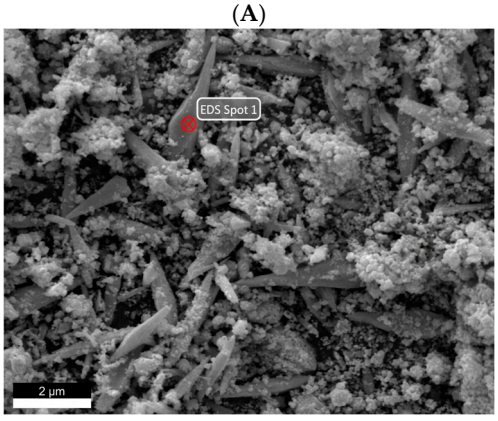

(**C**)

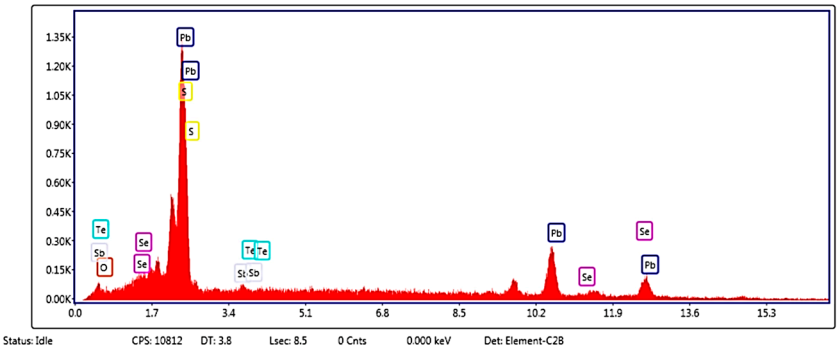

(**D**)

Figure 5. SEM imaging for spherical (**A**) and elongated (**C**) particles and respective peak diagrams (**B**,**D**) for sample number 10.

Table 7. EDS analysis of spherical and elongated particles of sample number 10.

Element		Pb	O	S	Se	Te	Sb
Wt(%)	**Spherical**	78.68	5.59	11.11	3.49	0.6	0.54
	Elongated	91.49	1.82	3.34	2.03	1.06	0.27

In Table 6, "nd" (or "Nd") denotes concentrations below the analytical limit of detection (LOD). Accordingly, the apparent non-monotonic variations in Te concentration after the initial period should be interpreted within analytical uncertainty rather than as a kinetically meaningful trend. Overall, Te dissolution appears to terminate early under the studied carbonate conditions, likely due to rapid surface passivation/product-layer formation, and therefore Te time profiles are discussed qualitatively.

As shown in Tables 5 and 6, under specific combinations of temperature and reagent concentration, selenium dissolution increases significantly, reaching a maximum value of approximately 33.9%. This behavior indicates that selenium release is not governed by simple diffusion-controlled dissolution but is strongly influenced by surface reactions and phase transformations occurring during leaching. In contrast, tellurium consistently shows lower dissolution efficiencies, remaining limited across all tested conditions, suggesting a higher degree of stabilization within the solid matrix.

The contrasting leaching responses of selenium and tellurium can be rationalized by considering their distinct chemical associations with lead-bearing phases. Figure 5 illustrates the evolution of particle surface morphology after leaching, revealing the formation of compact surface layers that partially encapsulate residual particles. Quantitative EDS results presented in Table 7 demonstrate an enrichment of lead and oxygen on particle surfaces following leaching, consistent with the precipitation of lead carbonate species. Such surface layers act as diffusion barriers, preferentially inhibiting the release of strongly associated chalcogen elements, particularly tellurium.

From a detoxification standpoint, this behavior is highly significant. The suppression of tellurium dissolution and the generally limited release of selenium imply that sodium carbonate leaching promotes immobilization rather than mobilization of hazardous chalcogen species. The occasional increase in selenium dissolution under specific conditions reflects localized disruption of surface layers rather than a fundamental change in leaching mechanism. Therefore, the process should be viewed as a controlled surface-mediated detoxification step rather than an aggressive extraction route.

Overall, the results presented in this section demonstrate that sodium carbonate leaching induces selective surface reactions leading to the formation of Pb-rich carbonate layers that regulate chalcogen release. This physically grounded understanding provides a coherent explanation for the quantitative trends observed in Tables 5 and 6 and establishes a direct link between microstructural evolution and detoxification performance.

3.3. Kinetic Interpretation and Rate-Controlling Step Analysis

To elucidate the rate-controlling mechanisms governing selenium leaching and tellurium immobilization during detoxification-oriented pre-treatment, kinetics analyses were carried out using both diffusion-based and nucleation-growth models. This comprehensive evaluation aimed to correlate the microstructural evolution of the lead-rich fly ash with its leaching behavior.

3.3.1. Comparative Model Fitting and Rate-Controlling Step Identification

To logically transition from observation to a physically constrained conclusion, the fractional conversion data (X) were fitted to the principal kinetic models. The quality of fit,

as quantified by the correlation coefficient (R^2) and standard deviation, is summarized in Table 8.

Figures 6 and 7 present the graphical manifestation of these fits. The temperature intervals used for devising these charts are 20 °C, 60 °C and 100 °C. It is evident from Figure 7 that the SCM diffusion model is statistically superior ($R^2 > 0.97$) to the other models. This superior fit is consistent with product-layer diffusion playing the dominant role in controlling the overall leaching rate under the studied conditions.

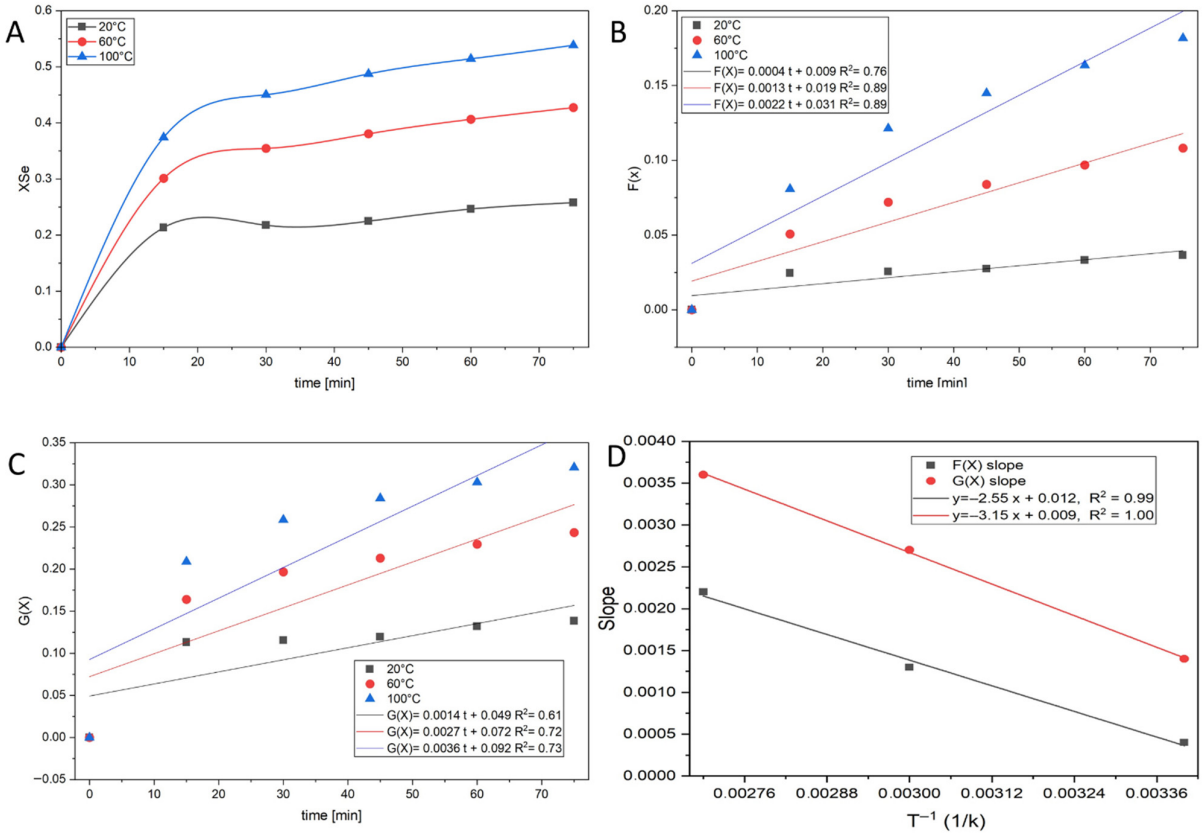

Figure 6. Se charts for the shrinking core model of elongated particles. Recovered Se vs. time (**A**), F(X) vs. time as for ash diffusion (**B**), G(X) vs. time as for chemical reaction (**C**), and Arrhenius plot of both vs. T^{-1} (**D**).

Table 8. Suggested models for prediction of kinetics control mechanisms [34].

Model	Rate Equation	R^2	Kinetic Stage Implied	Evidential Support
Surface Reaction Control	$1-(1-X)^{1/3}=k_s t$	0.85–0.92	Initial rapid stage	Early time points (Figure 8)
Product-Layer Diffusion (SCM)	$1-3(1-X)^{2/3}+2(1-X)=k_p t$	0.97–0.99	Dominant long-term stage	Figures 6 and 7 (linearity at high X)
Avrami Growth	$-\ln(1-X)=k_a t^n$	0.93–0.96	Nucleation/early growth	Early-to-intermediate conversion (Figure 8)

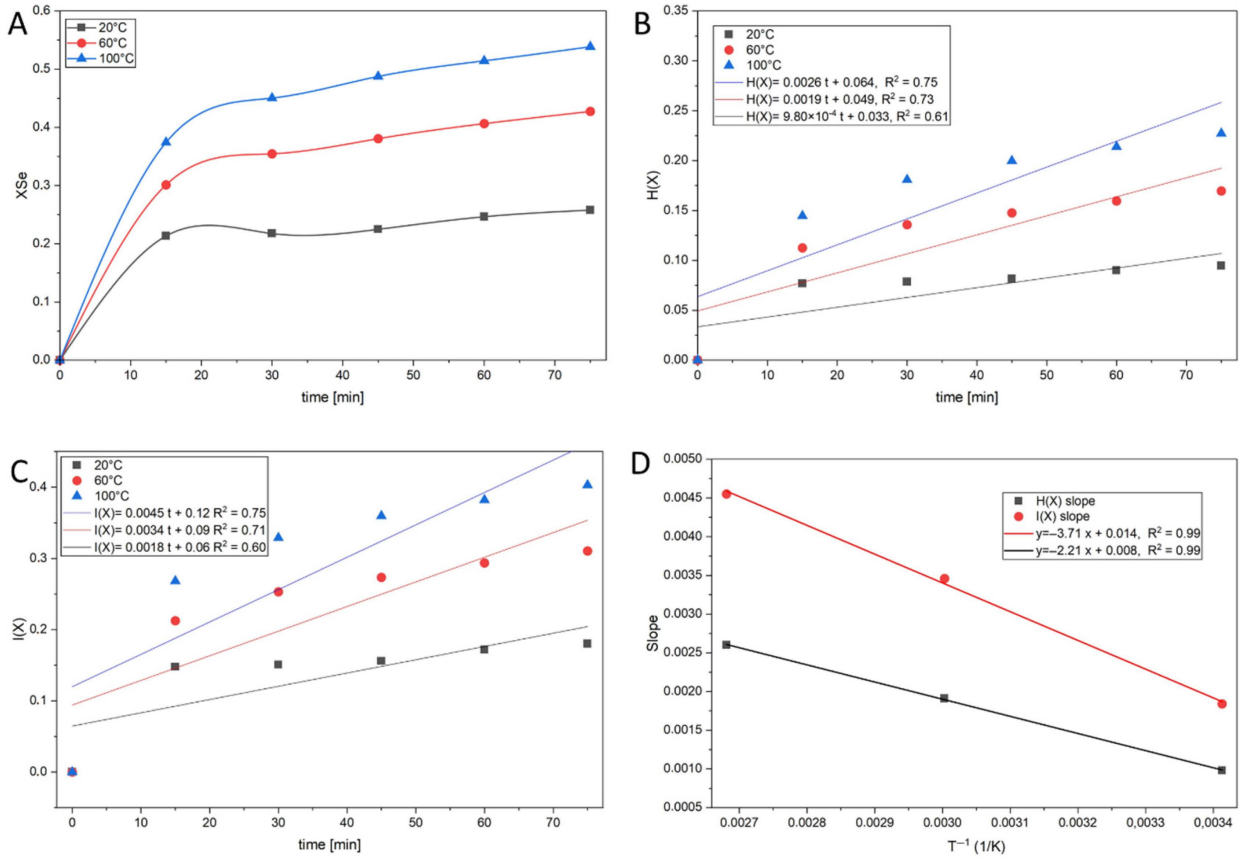

Figure 7. Se charts for the shrinking particle model of spherical particles. Recovered Se vs. time (**A**), H(X) vs. time as for film diffusion (**B**), I(X) vs. time as for chemical reaction (**C**), and Arrhenius plot of both vs. T^{-1} (**D**).

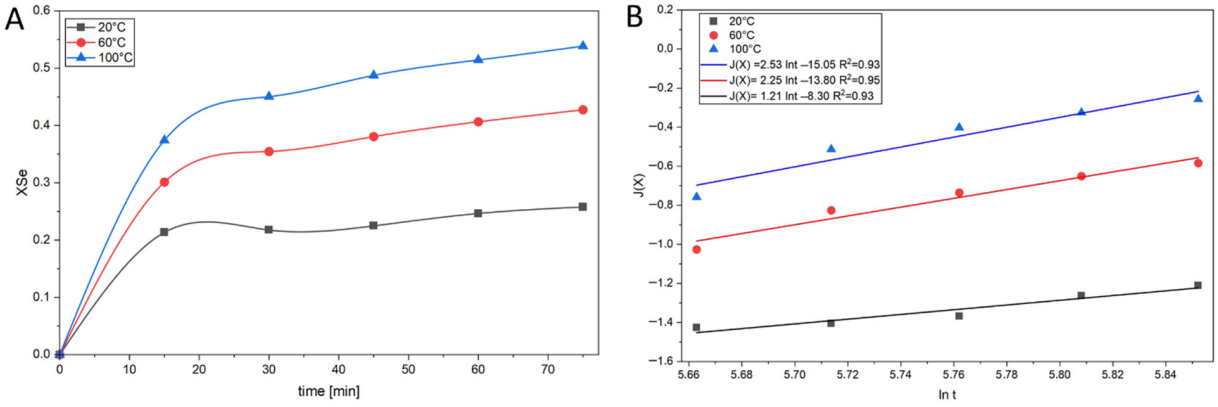

Figure 8. Se charts for the Avrami model. Recovered Se vs. time (**A**), J(X) vs. time (**B**).

3.3.2. Microstructural Validation and Mechanism Consolidation

The kinetic exponent (n) derived from the Avrami fit (using Figure 8) in the initial phase ($n \approx 1.1$–1.3) is consistent with a heterogeneous, two-dimensional growth mechanism for this layer, which subsequently transitions into a pure diffusion-controlled regime as the shell thickens and dominates the mass transport path. The kinetic evidence is strongly corroborated by the microstructural analysis presented in Figure 9 and the elemental mapping in Table 9. The formation of a dense, crystalline $PbCO_3$ phase—the primary component of the passivation layer—creates a physical barrier whose resistance is governed by the tortuosity and thickness of this layer, rather than the chemical reaction rate itself.

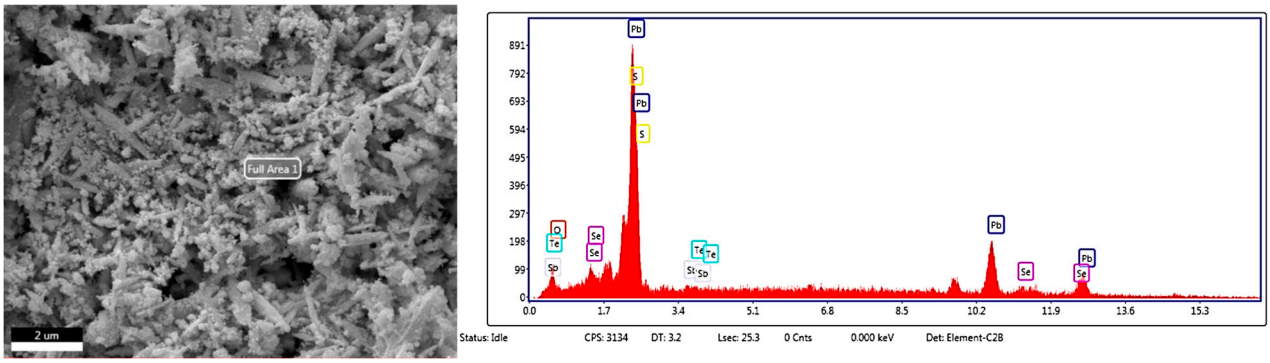

(**A**) (**B**)

Figure 9. SEM imaging (**A**) and peaks diagram (**B**) for sample number 17.

Table 9. EDS analysis of sample number 17.

Element	Pb	O	S	Se	Te	Sb
Wt (%)	82.96	6.27	4.56	5.39	0.35	0.47

Considering the inherent multi-phase and porous nature of the fly ash, the particles in this study are mathematically treated as pseudo-spherical entities. Consequently, the classical Shrinking Core Model (SCM) applied herein serves as an apparent kinetic model to macroscopically elucidate the rate-controlling steps of Se and Te dissolution. These microstructural and compositional observations provide direct physical validation for the diffusion-controlled SCM behavior identified earlier and simultaneously explain the observed kinetic selectivity between selenium and tellurium through preferential blockage of Te-bearing phases by the $PbCO_3$ product layer.

3.3.3. Physically Constrained Linkage Between Kinetic Parameters and RSM Optimization

The identification of diffusion-controlled kinetics through the shrinking core model (Section 3.3.1), together with its direct microstructural validation via $PbCO_3$ product layer formation (Section 3.3.2), provides a robust physically constrained basis for subsequent parametric optimization.

In this context, the apparent diffusion rate constant k_p (min^{-1}), extracted under different operating conditions, represents a physically meaningful response variable that inherently reflects the combined effects of temperature, solid-to-liquid ratio, and leaching time.

Rather than relying solely on empirical recovery values, the response surface methodology (RSM) employed in Section 3.4 utilizes these kinetically grounded parameters to map the multidimensional process space. This approach ensures that the statistically optimized conditions remain consistent with the established rate-controlling mechanism, thereby preventing nonphysical optimization outcomes that contradict diffusion limitations imposed by the $PbCO_3$ layer.

3.4. Parametric Study and Statistical Optimization (RSM)

3.4.1. Experimental Design and Definition of the Kinetic Response

In order to quantitatively optimize the detoxification-oriented leaching process while remaining consistent with the established diffusion-controlled mechanism, a response surface methodology (RSM) was employed. The experimental matrix was constructed using the same operational domain investigated in the kinetic analysis, ensuring direct compatibility between physically constrained interpretation and statistical modeling.

Temperature, solid-to-liquid ratio, and leaching time were selected as independent variables based on their demonstrated influence on product layer development and diffu-

sion resistance. Importantly, the apparent diffusion rate constant k_p, extracted from the shrinking core model analysis (Section 3.3), was defined as the primary response variable. This choice avoids purely empirical optimization based on extraction yield and instead anchors the statistical analysis to a physically meaningful kinetic descriptor of the process.

The experimental runs generated a sufficient data set to capture both linear and interaction effects among the operating variables within the diffusion-controlled regime.

3.4.2. Model Fitting and Statistical Validation

The experimental responses were fitted using a second-order polynomial model, and the adequacy of the proposed regression was evaluated through standard statistical indicators. The CCD design with 24 factorial points and six center points provides sufficient resolution to capture both linear and interaction effects among the variables. The resulting model coefficients and significance of fit parameters are summarized in Tables 10 and 11, demonstrating satisfactory agreement between predicted and experimental values.

Table 10. Full data set for Design Expert 12.

	Na_2CO_3 Conc	Temperature	Solid-to-Liquid Ratio	Time	Se Extraction	Te Extraction	Se Concentration	Te Concentration
Run	**(mol/L)**	**(°C)**	**(gr/mL)**	**(Minute)**	**(%)**	**(%)**	**(ppm)**	**(ppm)**
1	0.3	80	0.1	30	28.03	2.68	501.75	24.00
2	0.5	60	0.075	45	33.13	12.70	444.75	85.25
3	0.7	40	0.05	45	34.64	13.58	310.00	60.75
4	0.7	40	0.1	60	28.66	6.12	513.00	54.75
5	0.7	40	0.05	60	39.89	17.60	357.00	78.75
6	0.3	80	0.1	60	29.30	1.79	524.50	16.00
7	0.3	40	0.1	30	20.21	0.00	361.75	0.00
8	0.5	20	0.075	45	22.48	0.71	301.75	4.75
9	0.5	60	0.125	45	34.66	3.06	775.50	34.25
10	0.1	60	0.075	45	17.90	0.93	240.25	6.25
11	0.7	80	0.05	30	42.88	23.24	383.75	104.00
12	0.9	60	0.075	45	38.96	15.98	523.00	107.25
13	0.3	40	0.05	60	23.18	3.58	207.60	16.00
14	0.5	60	0.075	15	30.11	9.35	404.25	62.75
15	0.5	60	0.075	45	45.81	18.70	615.00	125.50
16	0.5	60	0.025	45	47.99	36.31	214.75	81.25
17	0.7	80	0.1	60	49.85	19.50	892.25	174.50
18	0.7	80	0.05	60	51.12	33.69	457.50	150.75
19	0.5	100	0.075	45	48.75	13.30	654.50	89.25
20	0.7	80	0.1	30	42.67	16.23	763.75	145.25
21	0.5	60	0.075	75	42.18	11.32	566.25	76.00
22	0.5	60	0.075	45	38.79	13.59	520.75	91.25
23	0.7	40	0.1	30	23.24	5.08	416.00	45.50
24	0.5	60	0.075	45	35.87	10.61	481.50	71.25
25	0.3	80	0.05	60	42.35	17.60	379.00	78.75
26	0.3	40	0.05	30	20.73	4.02	185.50	18.00
27	0.5	60	0.075	45	38.06	9.94	511.00	66.75
28	0.3	80	0.05	30	36.96	15.20	330.75	68.00
29	0.5	60	0.075	45	35.85	8.57	481.25	57.50
30	0.3	40	0.1	60	23.35	0.00	418.00	0.00

The CCD–RSM analysis is used here as a statistical screening framework to rank the relative influence of operating parameters and their interactions on the responses, while acknowledging that precipitation/passivation phenomena may limit strict first-principles interpretation of the fitted terms.

Table 11. Full ANOVA table for all 4 responses.

Model	Se						Te					
	Recovery			Concentration			Recovery			Concentration		
	Sum of Squares	F-Value	*p*-Value	Sum of Squares	F-Value	*p*-Value	Sum of Squares	F-Value	*p*-Value	Sum of Squares	F-Value	*p*-Value
Linear												
Time (t)	162.7	10.4	0.006	27,989.3	8.3	0.011	23.5	1.7	0.208	709.6	1.6	0.227
Temperature (T)	1090.8	69.8	<0.0001	1.96×10^5	58.5	<0.0001	460.4	33.8	<0.0001	17,958.0	40.1	<0.0001
$[Na_2CO_3]$ (C)	714.4	45.7	<0.0001	1.28×10^5	38.0	<0.0001	602.6	44.3	<0.0001	26,367.5	58.9	<0.0001
S/L	222.6	14.2	0.0018	3.51×10^5	104.6	<0.0001	859.3	63.1	<0.0001	1820.0	4.0	0.062
Quadratic												
t^2	15.2	0.975	0.339	2570.8	0.766	0.395	7.6	0.557	0.467	135.7	0.303	0.590
T^2	21.1	1.4	0.263	3603.8	1.1	0.316	50.6	3.7	0.073	1676.3	3.7	0.072
C^2	196.2	12.6	0.003	34,737.5	10.4	0.006	27.2	2	0.178	794.0	1.8	0.203
S/L^2	8.3	0.529	0.48	1426.8	0.425	0.524	90.1	6.6	0.021	721.9	1.6	0.224
Interactive												
t × T	2.1	0.135	0.719	161.9	0.048	0.829	7.0	0.517	0.483	178.9	0.399	0.537
t × C	12.0	0.765	0.396	2423.1	0.722	0.409	19.6	1.4	0.249	656.6	1.5	0.245
t × S/L	1.2	0.075	0.788	803.7	0.24	0.632	10.6	0.778	0.392	115.6	0.26	0.619
T × C	7.5	0.477	0.501	7144.5	2.1	0.165	26.6	1.95	0.183	2070.2	4.62	0.048
T × S/L	0.0144	0.0009	0.9762	14,556.42	4.3	0.0548	30.1	2.2	0.1573	62.0	0.138	0.71
C × S/L	0.199	0.013	0.912	8723.6	2.6	0.128	1.7	0.126	0.727	1732.6	3.9	0.07

Analysis of variance (ANOVA), as presented in Table 11, confirmed the statistical significance of the quadratic model ($p < 0.05$) for the selected variables, and residual analysis indicated no obvious deviation from normality or homoscedasticity within the studied design space, confirming the statistical significance of the regression model within a 95% confidence level (R^2 values presented in Table 12), with temperature emerging as the dominant factor influencing the diffusion rate constant. This observation is fully consistent with the physically constrained framework established earlier, where increased temperature enhances ionic mobility through the $PbCO_3$ product layer while preserving the diffusion-controlled nature of the process. Interaction terms between temperature and solid-to-liquid ratio further indicate that mass transfer resistance within the product layer is sensitive to both thermal activation and solution availability. The coded coefficient of parameters presented in Table 13 shows the expected change in response per unit change in factor value when all remaining factors are held constant. Therefore, indicating the contribution scale of each factor.

Table 12. R-squared values for all responses.

Response	R^2	Adjusted R^2	Predicted R^2
Se recovery	0.88	0.86	0.82
Te recovery	0.85	0.81	0.71
Se concentration	0.90	0.88	0.84
Te concentration	0.72	0.70	0.66

From a metallurgical perspective, the significant interactive effects observed between temperature and lixiviant concentration (T × C) statistically validate the proposed apparent kinetic model. As the temperature increases, the kinetic bottleneck transitions, amplifying the role of reagent diffusion through the porous solid product layer, which inherently depends on the bulk concentration of the carbonate ions.

Table 13. Coded coefficient of parameters for all 4 equations.

Factors		Time	Temperature	$[Na_2CO_3]$	s/L	$[Na_2CO_3]^2$	(s/L) × Temperature	$(s/L)^2$	Intercept
Coefficients	Se Recovery	2.6	6.74	5.46	−3.05	−2.56	-	-	36.96
	[Se]	34.15	90.41	72.91	120.89	32.44	30.16	-	483.84
	Te Recovery	-	4.38	5.01	−5.98	-	-	2.13	9.79
	[Te]	-	27.35	33.15	-	-	-	-	66.48

The normal probability distribution of residuals and parity plots shown in Figure 10 further validate the robustness of the fitted model, confirming that no systematic deviation from the assumed kinetic behavior is introduced by the statistical treatment. In these plots, an increase in temperature makes the solid-to-liquid ratio more potent. This may be the result of higher ion mobility due to higher temperature.

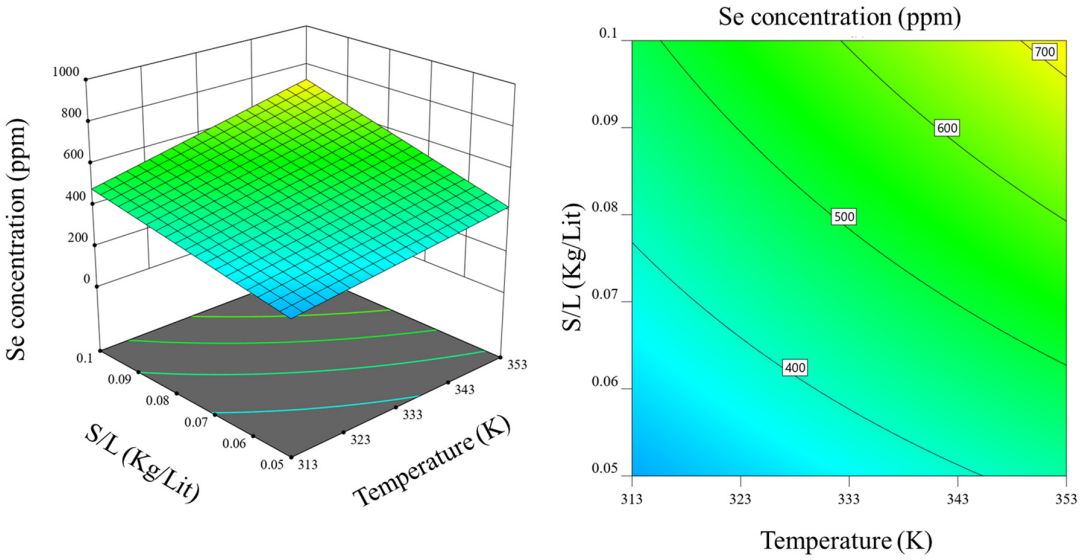

Figure 10. Response surface plot and contour plot of factor interactions of temperature relative to solid-to-liquid ratio for Se concentration. Both Na_2CO_3 concentration and time have been fixed to the central value.

4. Conclusions

This study clarified the detoxification-oriented leaching behavior of selenium and tellurium from lead-rich fly ash through an integrated microstructural–kinetic–statistical framework, beginning with characterization that revealed heterogeneous Pb-bearing matrices and chalcogenide-rich phases, supported by quantitative particle-size analysis using ImageJ. Leaching tests showed strong selectivity toward selenium dissolution, while tellurium extraction remained limited due to fundamentally different transport behaviors in the evolving solid matrix. Kinetic evaluation indicated an initial nucleation-controlled stage followed by a dominant diffusion-controlled regime consistent with the shrinking-core model, with SEM–EDS confirming the formation of a compact $PbCO_3$ product layer that imposes the primary diffusion barrier, particularly restricting tellurium transport—an outcome consistent with observations reported by Xu [23], Kurniawan [24], and Chen [25]. Statistical optimization, performed using response surface methodology and constrained by a physically informed linkage between operating variables and the apparent diffusion rate constant k_p, ensured adherence to the diffusion-controlled mechanism and avoided unrealistic yield-based maxima. The optimal operating window thus reflects conditions

that enhance diffusion kinetics without destabilizing the governing product layer. Overall, this work shows that effective statistical optimization of detoxification processes must be grounded in kinetic interpretation and microstructural validation, offering a rational basis for designing leaching strategies for complex secondary resources where detoxification performance is controlled by transport limitations within evolving solid phases. From an environmental and kinetic perspective, the alkaline carbonate medium not only facilitated the selective recovery of Se and Te but also inherently detoxified the final residue. The formation of a highly insoluble $PbCO_3$ product layer (K_sp $\approx 7.4 \times 10^{-14}$) thermodynamically effectively immobilized secondary lead emissions, while concurrently acting as a diffusion barrier modeled through an apparent pseudo-spherical SCM approach. Additionally, it appears that studying a wider range of parameters for leaching, checking the synergistic effects of some additives such as sodium sulfide and further separation and production of Se and Te downstream, can provide insightful improvements to future studies of this scope. While the current thermodynamic and kinetic evaluations strongly indicate improved environmental stability of the residue, future studies should incorporate standard environmental leaching protocols, such as the Toxicity Characteristic Leaching Procedure (TCLP), to fully validate its long-term safety for disposal.

Author Contributions: M.R.A.: software, validation, formal analysis, investigation, data curation, writing—original draft preparation, writing—review and editing, visualization; A.M.B.: conceptualization, methodology, validation, writing—original draft preparation, writing—review and editing, supervision; E.K.A.: conceptualization, methodology, validation, resources, writing—review and editing, supervision, project administration, funding acquisition. All authors have read and agreed to the published version of the manuscript.

Funding: This research received no external funding.

Data Availability Statement: The data presented in this study are available on request from the corresponding author. The data are not publicly available due to privacy.

Conflicts of Interest: The authors declare no conflicts of interest.

Appendix A. Comparison of Extraction Routes

Table A1. Comparative analysis of pyrometallurgical and hydrometallurgical routes for the extraction of Se and Te from secondary resources (e.g., copper anode slime and fly ash) *.

Parameter	Pyrometallurgical Routes	Hydrometallurgical Routes
OperatingPrinciple	Roasting, smelting, or volatilization at high temperatures.	Selective dissolution (leaching) in aqueous solutions.
Temperature	Very high (typically > 600 °C).	Low to moderate (typically < 100 °C).
Energy Consumption	High, due to significant furnace heating requirements.	Significantly lower, driven by chemical potential rather than heat.
Reagents	Fluxes (e.g., Na_2CO_3, SiO_2) and solid reductants.	Acids, bases, or oxidants (e.g., H_2SO_4, NaOH, Na_2CO_3).
Selectivity	Generally lower; trace elements may report to multiple phases (slag, gas, matte).	Higher potential for selective extraction through targeted pH and potential (Eh) control.
Environmental Impact	High risk of hazardous emissions (SO_2 gas, volatile Se/Te, dust).	Generally contained liquid effluents requiring standard neutralization.
Process Control	Kinetics governed by high-temperature phase equilibria.	Highly controllable parameters (temperature, pH, reagent concentration).

* Note: This comparative summary is compiled based on established fundamental principles of extractive metallurgy and the background literature discussed in the Section 1 of this study.

References

1. Mahmoudi, A.; Shakibania, S.; Mokmeli, M.; Rashchi, F. Tellurium, from Copper Anode Slime to High Purity Product: A Review Paper. *Metall. Mater. Trans. B Process Metall. Mater. Process. Sci.* **2020**, *51*, 2555–2575. [CrossRef]
2. Fthenakis, V.; Athias, C.; Blumenthal, A.; Kulur, A.; Magliozzo, J.; Ng, D. Sustainability evaluation of CdTe PV: An update. *Renew. Sustain. Energy Rev.* **2020**, *123*, 109776. [CrossRef]
3. Li, Z.; Qiu, F.; Tian, Q.; Yue, X.; Zhang, T. Production and recovery of tellurium from metallurgical intermediates and electronic waste-A comprehensive review. *J. Clean. Prod.* **2022**, *366*, 132796. [CrossRef]
4. Hoffmann, J.E. Recovering selenium and tellurium from copper refinery slimes. *JOM* **1989**, *41*, 33–38. [CrossRef]
5. Adriano, D.C. *Trace Elements in the Terrestrial Environment*; Springer: Berlin/Heidelberg, Germany, 1986.
6. Hait, J.; Jana, R.K.; Sanyal, S.K. Processing of copper electrorefining anode slime: A review. *Miner. Process. Extr. Metall.* **2009**, *118*, 240–252. [CrossRef]
7. Chen, T.T.; Dutrizac, J.E. Mineralogical characterization of anode slimes-II. Raw anode slimes from inco's copper cliff copper refinery. *Can. Metall. Q.* **1988**, *27*, 97–105. [CrossRef]
8. Fan, Y.; Yang, Y.; Xiao, Y.; Zhao, Z.; Lei, Y. Recovery of tellurium from high tellurium-bearing materials by alkaline pressure leaching process: Thermodynamic evaluation and experimental study. *Hydrometallurgy* **2013**, *139*, 95–99. [CrossRef]
9. Li, Z.; Liu, D.; Zha, G.; Jiang, W.; Huang, D.; Xu, B. Efficient Separation and Recovery of Tellurium and Copper from High—Value—Added Industrial Copper Telluride Slag by a Sustainable Process. *J. Sustain. Metall.* **2023**, *9*, 738–752. [CrossRef]
10. Sarangi, C.K.; Sheik, A.R.; Marandi, B.; Ponnam, V.; Ghosh, M.K.; Sanjay, K.; Minakshi, M.; Subbaiah, T. Recovery of Tellurium from Waste Anode Slime Containing High Copper and High Tellurium of Copper Refineries. *Sustainability* **2023**, *15*, 11919. [CrossRef]
11. Mahmoudi, A.; Shakibania, S.; Mokmeli, M.; Rashchi, F.; Karimi, H.Y. Selective Separation and Recovery of Tellurium from Copper Anode Slime Using Acidic Leaching and Precipitation with Cuprous Ion. *J. Sustain. Metall.* **2021**, *7*, 1886–1898. [CrossRef]
12. Rao, S.; Liu, Y.; Wang, D.; Cao, H.; Zhu, W.; Yang, R.; Duan, L.; Liu, Z. Pressure leaching of selenium and tellurium from scrap copper anode slimes in sulfuric acid-oxygen media. *J. Clean. Prod.* **2021**, *278*, 123989. [CrossRef]
13. Zhen, T.; Luo, H.; Liu, L.; Zha, G.; Yang, B.; Jiang, W.; Xu, B. Selective Recovery of Valuable Metals (Se, Te, Cu) from the Selenium Distillation Residue by Sulfuric Acid Oxidative Leaching. *J. Sustain. Metall.* **2022**, *8*, 1191–1203. [CrossRef]
14. Shao, L.; Diao, J.; Hu, R.; Ji, C.; Tan, W.; Li, H.; Xie, B. Dissolution Behaviors of Minerals in Tellurium—Bismuth Ore During Oxidic—Acidic Leaching. *J. Sustain. Metall.* **2021**, *7*, 1790–1804. [CrossRef]
15. Dong, Z.; Jiang, T.; Xu, B.; Yang, J.; Chen, Y.; Li, Q.; Yang, Y. Comprehensive recoveries of selenium, copper, gold, silver and lead from a copper anode slime with a clean and economical hydrometallurgical process. *Chem. Eng. J.* **2020**, *393*, 124762. [CrossRef]
16. Zeng, H.; Liu, F.; Zhou, S.; Liao, C.; Chen, F.; Zeng, Y. Leaching Behavior of the Main Metals from Copper Anode Slime during the Pretreatment Stage of the Kaldor Furnace Smelting Process. *Processes* **2022**, *10*, 2510. [CrossRef]
17. Kilic, Y.; Kartal, G.; Timur, S. An investigation of copper and selenium recovery from copper anode slimes. *Int. J. Miner. Process.* **2013**, *124*, 75–82. [CrossRef]
18. González-Ibarra, A.A.; Nava-Alonso, F.; Dávila-Pulido, G.I.; Carrillo-Pedroza, F.R.; Rodríguez-Flores, A.M. Dissolution behavior of elemental tellurium and tellurium dioxide in alkaline cyanide solutions. *Hydrometallurgy* **2021**, *203*, 105702. [CrossRef]
19. Guo, X.; Xu, Z.; Li, D.; Tian, Q.; Xu, R.; Zhang, Z. Recovery of tellurium from high tellurium-bearing materials by alkaline sulfide leaching followed by sodium sulfite precipitation. *Hydrometallurgy* **2017**, *171*, 355–361. [CrossRef]
20. Xu, L.; Xiong, Y.; Zhang, G.; Zhang, F.; Yang, Y.; Hua, Z.; Tian, Y.; You, J.; Zhao, Z. An environmental-friendly process for recovery of tellurium and copper from copper telluride. *J. Clean. Prod.* **2020**, *272*, 122723. [CrossRef]
21. Yang, H.Y.; Li, X.J.; Tong, L.L.; Jin, Z.N.; Yin, L.; Chen, G.B. Leaching kinetics of selenium from copper anode slimes by nitric acid-sulfuric acid mixture. *Trans. Nonferrous Met. Soc. China (Engl. Ed.)* **2018**, *28*, 186–192. [CrossRef]
22. Pan, X.; Hong, Y.; Hu, T.; Zhang, L.; Yang, K. Kinetic mechanism of selenium leaching from selenium-rich acid sludge in NaOH solution. *Can. Metall. Q.* **2023**, *63*, 563–575. [CrossRef]
23. Xu, Z.; Guo, X.; Li, D.; Tian, Q. Leaching kinetics of tellurium-bearing materials in alkaline sulfide solutions. *Miner. Process. Extr. Metall. Rev.* **2020**, *41*, 1–10. [CrossRef]
24. Kurniawan, K.; Lee, J.; Kim, J.; Kim, R.; Kim, S. Leaching Kinetics of Selenium, Tellurium and Silver from Copper Anode Slime by Sulfuric Acid Leaching in the Presence of Manganese (IV) Oxide and Graphite †. *Mater. Proc.* **2021**, *3*, 16.
25. Chen, J.; Liu, Z.; Wang, Q.; Wang, S.; Guo, X. Kinetics of tellurium recovery by sodium sulfide leaching from copper anode slime. *Sep. Purif. Technol.* **2026**, *380*, 135249. [CrossRef]
26. Moosavi-Khoonsari, E.; Tripathi, N. Copper Anode Slime Processing with a Focus on Gold Recovery: A Review of Traditional and Recent Technologies. *Processes* **2024**, *12*, 2686. [CrossRef]
27. World Health Organization. Lead Poisoning. 2024. Available online: https://www.who.int/news-room/fact-sheets/detail/lead-poisoning-and-health?utm_source=chatgpt.com (accessed on 13 November 2025).

28. National Center for Biotechnology Information (NCBI). *Agency for Toxic Substances and Disease Registry, Toxicological Profile for Selenium: Relevance to Public Health*; National Center for Biotechnology Information (NCBI): Bethesda, MD, USA, 2003. Available online: https://www.ncbi.nlm.nih.gov/books/NBK600362/?utm_source=chatgpt.com (accessed on 13 November 2025).
29. Lenntech, B.V. Tellurium (Te)—Chemical Properties, Health and Environmental Effects. Available online: https://www.lenntech.com/periodic/elements/te.htm?utm_source=chatgpt.com (accessed on 13 November 2025).
30. Arai, K.; Toguri, J.M. Leaching of lead sulphate in sodium carbonate solution. *Hydrometallurgy* **1984**, *12*, 49–59. [CrossRef]
31. Lindquist, B.K.; Petersson, S.A.; Boliden, A.B. Lindquist, Method for Producing Metallic Lead by Direct Lead-Smelting. U.S. Patent 4,584,017, 22 April 1986.
32. Movahhedi, H.; Beygian, A.M.; Keshavarz, E. Developing of a Counter-Current Copper Leaching Process Using Response Surface Methodology Developing of a Counter-Current Copper Leaching Process Using Response Surface. *Miner. Process. Extr. Metall. Rev.* **2023**, *45*, 824–834. [CrossRef]
33. Hesar, A.O.; Beygian, A.M.; Keshavarz, E.; Allahyari, J.; Moradi, A. Investigation of Aldoxime-Ketoxime Solvent Mixtures for Selective Copper Extraction: In-Depth Performance Evaluation Through RSM, Slope Method Mechanism Determination, Ex (%)-pH and McCabe-Thiele Diagrams Investigation of Aldoxime-Ketoxime Solvent Mixt. *Solvent Extr. Ion Exch.* **2025**, *43*, 267–293. [CrossRef]
34. Levenspiel, O. *Chemical Reaction Engineering*; John Wiley & Sons: Hoboken, NJ, USA, 1998.

Disclaimer/Publisher's Note: The statements, opinions and data contained in all publications are solely those of the individual author(s) and contributor(s) and not of MDPI and/or the editor(s). MDPI and/or the editor(s) disclaim responsibility for any injury to people or property resulting from any ideas, methods, instructions or products referred to in the content.